Energy and AI 2 (2020) 100032

Contents lists available at ScienceDirect

Energy and AI

journal homepage: www.elsevier.com/locate/egyai

A modeling and experimental study of capacity fade for lithium-ion batteries

Andrew Carnovale, Xianguo Li*

Department of Mechanical and Mechatronics Engineering, University of Waterloo, Waterloo, Ontario N2L 3G1, Canada

HIGHLIGHTS

- Developed a first-principle-based predictive model for Li-ion battery capacity fade.
- Incorporated mechanisms of degradation at different battery operation temperature.
- Conducted experimental measurements of battery capacity fade.
- Found good agreement between the model prediction and experimental results.

GRAPHICAL ABSTRACT

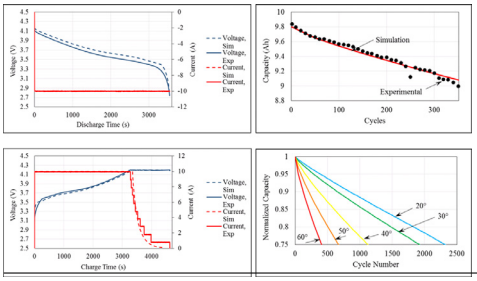

ARTICLE INFO

Article history:
Received 26 August 2020
Received in revised form 7 October 2020
Accepted 8 October 2020
Available online 10 October 2020

Keywords:
Lithium-ion batteries
Capacity fade
Degradation
Aging
Modeling
Experiment

ABSTRACT

Lithium-ion batteries are extensively used in electric vehicles, however, their significant degradation over discharge and charge cycles results in severe capacity fade, limiting driving ranges of electric vehicles over time and useful lifetime of batteries. In this study, capacity fade for lithium-ion battery has been investigated through modeling and experiment. A predictive model is developed based on first principles incorporating degradation mechanisms. The mechanisms of degradation considered include solid-electrolyte interface (SEI) growth and active material loss at both negative and positive electrodes. Battery performance including capacity is measured experimentally under discharge and charge cycling with battery operation temperature controlled. It is shown that battery capacity is reduced over battery discharge/charge cycling at a given battery operation temperature, and the model predicted battery performance, including capacity fade, agrees well with the experimental results. As the number of discharge/charge cycles are increased, battery capacity is reduced significantly; battery capacity fade is increased substantially when battery operation temperature is increased, indicating significantly accelerated aging of the battery at elevated operation temperatures and hence the importance of battery thermal management in the control of battery operation temperature for practical applications such as electric vehicles. Battery capacity fade is mainly caused by SEI film growth at the negative electrode, which is the largest contributing factor to the capacity fade, and the active material isolation at the negative electrode, which is the second largest influencing aging factor.

1. Introduction

Electrification of transportation sector has been intensifying as a response to the global climate change, and battery electric (and hybrid) vehicles have seen significant increase in the recent decades, partly also because of the ease in powering sensing, control, regenerative braking for energy recovery and storage, as well as smart and autonomous driving systems. Lithium-ion batteries are seen as the superior choice in battery technology due to their high energy and power densities [1–3]. However, a key technical challenge to the current battery technology is its performance over long cycling periods, commonly referred to as battery capacity fade, or the loss of usable energy from a battery at the increased number of discharge/charge cycles. This limits the driving range between the charge, the lifetime of battery, and the excessive number and weight of batteries used for automobiles. Further, battery performance is the best around the temperature of 25–30 °C, and deteriorates significantly when battery operation temperature is higher or lower; while automobiles can experience all weather/temperature condition depending on the time of the day and the season of the year dur-

* Corresponding author.
E-mail address: x6li@uwaterloo.ca (X. Li).

https://doi.org/10.1016/j.egyai.2020.100032

ing its lifetime. Therefore, thermal management becomes key to prevent the permanent loss of battery capacity, and safe operation of lithium-ion batteries preventing thermal runaway, caused by high cell temperature, which can often lead to fires and explosions [3, 4]. An appropriate strategy for thermal management depends on the knowledge of the effect of battery operation temperature on the battery performance degradation leading to capacity fade.

Many studies have been carried out in the area of lithium-ion battery degradation (or aging) mechanisms resulting in capacity fade. Arora et al. [5] reported a multitude of degradation mechanisms that cause capacity fade in lithium-ion batteries. They reported side reactions, which occur due to overcharging, can cause metallic lithium formation at the negative electrode, unwanted inert materials at the positive electrode, or oxidation/reduction of the electrolyte, all of which can lead to loss of lithium or active material, leading to capacity fade. Further, they discussed film formation at both electrodes, indicating a passive interfacial layer will form on electrodes (the so-called solid-electrolyte interface, or SEI), protecting the electrode material, even though it causes an initial loss of lithium [5, 6]. Other mechanisms discussed by Arora et al. include corrosion and pitting of aluminum and copper current collector, and dissolution of the positive electrode into the electrolyte.

A wide range of aging mechanisms affecting lithium-ion batteries has been investigated. Aurbach et al. [7] reviewed mechanisms that affect anodes of either lithium metal or graphite composition, and concluded that lithium metal batteries subject to high charge rates would exhibit very poor life performance. On top of SEI layer growth, they indicated that exfoliated graphite particles due to the interaction with solvent molecules, and electrical isolation of graphite particles due to film growth can become issues for graphite anodes. Broussely et al. [8] again indicated that while excessive SEI layer growth leads to significant capacity loss, a stable SEI layer can lead to a battery with minimal capacity loss; and that the most rapid capacity loss is a result of lithium plating on the electrodes. Vetter et al. [9] conducted a comprehensive review of lithium-ion battery degradation mechanisms, including SEI growth (enhanced at high temperatures), cracking active material particles enhanced with overcharge, detachment of active material particles due to volume changes enhanced with cycling, decomposition of the electrode binder enhanced at high temperatures, and plating of metallic lithium which is enhanced at low temperatures. They noted that nickel-cobalt oxide cathodes tend to not experience dissolution unless charged to excessively high potential, however, nickel-cobalt cathodes are susceptible to film formation. They also reported that manganese cathodes are prone to dissolution where active manganese (Mn(III)) is lost.

Bro and Levy suggested a very early and simple model to describe the loss of battery capacity over time, a simple Arrhenius relation without taking into account any specific degradation mechanism [10]. Ramadass et al. carried out experiments to characterize capacity fade at elevated temperatures, and reported that the majority of capacity fade was due to loss of electrode active material (carbon anode, and $LiCoO_2$ cathode) compared to the loss of lithium [11, 12]. However, at high temperatures, lithium loss due to film formation at the anode become a significant source of capacity fade [12]. Ramadass et al. developed a semi-empirical model to predict capacity fade [13]. Similar work was carried out to predict battery life when lithium-ion batteries were cycled, with studies on SEI layer formation [14]. Spotnitz presented multiple methods of modeling the effect the SEI layer has on capacity loss, including models considering irreversible and reversible losses, and capacity loss due to SEI dissolution (oppose to just the growth of SEI) [15]. Liaw et al. used an alternate approach to model battery performance, using a simple equivalent circuit model, and incorporating thermal aging, but all nonlinear impedances used in the model were empirically determined [16].

Ramadass et al. [17] developed a capacity fade model to study the effect of parameters on capacity fade, which was assumed to occur only at the negative electrode during charge periods through the formation of a continuous SEI film around the active material. The resistance loss of this SEI film was considered responsible for the capacity fade, while the thickness of the SEI film was modeled for its growth (and lithium consumption). Vazuqez-Arenas et al. have also modelled capacity fade attributed to SEI formation, while also including volume changes of the positive electrode due to dissolution of the positive active material ($Li_yMn_2O_4$) [18].

A more detailed model of capacity fade due to SEI film formation was developed by Deshpande et al., attributing the degradation to enhanced SEI film formation as a result of physical damage via fatigue and cracking to the negative active material [19]. This model assumed that the SEI would crack as a result of fatigue due to volume changes of the active material during operation; these cracks would lead to exposed active material, leading to further SEI film growth [19]. This model coupled the growth of SEI layer due to chemical side reactions to physical fatigue mechanics to model capacity fade [19]. Another study by Cai et al. focused on degradation at the cathode [20]. Specifically the dissolution of Mn of a $LiMnO_2$ cathode. The model assumed that Mn phases cause degradation at both electrodes [20]. Mn^{2+} ions dissolve into the electrolyte and may transfer to and deposit on the anode leading to anode degradation, while solid and inert Mn metal remains at the cathode; both of these also lead to direct loss of useable Mn at the cathode [20]. Smith et al. studied SEI growth experimentally under a variety of cell operating conditions [21]. They concluded that time (opposed to cycle count) and temperature are the main factors leading to SEI growth, and suggested decreasing the negative electrode surface area to reduce SEI layer development [21]. Amine et al. studied capacity fade mechanisms of a lithium-ion cell with an NMC cathode and graphite anode at elevated temperatures [22]. They concluded that the main cause for degraded performance is dissolved metals from the cathode depositing on the anode, and suggested using an electrolyte additive to mitigate this degradation [22]. A recent review [23] summarizes the latest understanding of SEI formation, growth and impact on battery performance and performance degradation.

It is clear from the above review of pertinent literature that there is an urgent need to develop a first-principles based predictive model for the performance loss of Lithium-ion battery, incorporating all the essential chemical and physical processes involved, including both chemical kinetics at the electrodes and physical processes related to transport phenomena of heat and species; the predictive model should be sufficiently simple for fast analysis, and should be validated against experimental results for accuracy required for practical engineering application, such as for the proper design of battery thermal management in practical electric vehicles. Therefore, the objective of the present study is to develop a predictive model for battery capacity fade for a range of battery operation temperatures under discharge/charge cycling, and such a predictive model should have reasonable accuracy with less computational complexity for practical purpose, and should be validated by experimental results for its accuracy and reliability. In this study, the predictive model is developed based on the first principles with performance degradation mechanisms integrated, and an associated experimental measurement is carried out to provide data for model validation. The validated model will be useful for assessment of performance fade under different battery operation temperatures and discharge/charge cycling, thus yielding an estimate of battery lifetime or remaining useful life.

2. Model formulation

As mentioned above, the physical problem considered in the present study is the degradation of lithium-ion batteries over discharge/charge cycling at different operation temperatures. This entails operating a battery under set conditions including a specified battery operation temper-

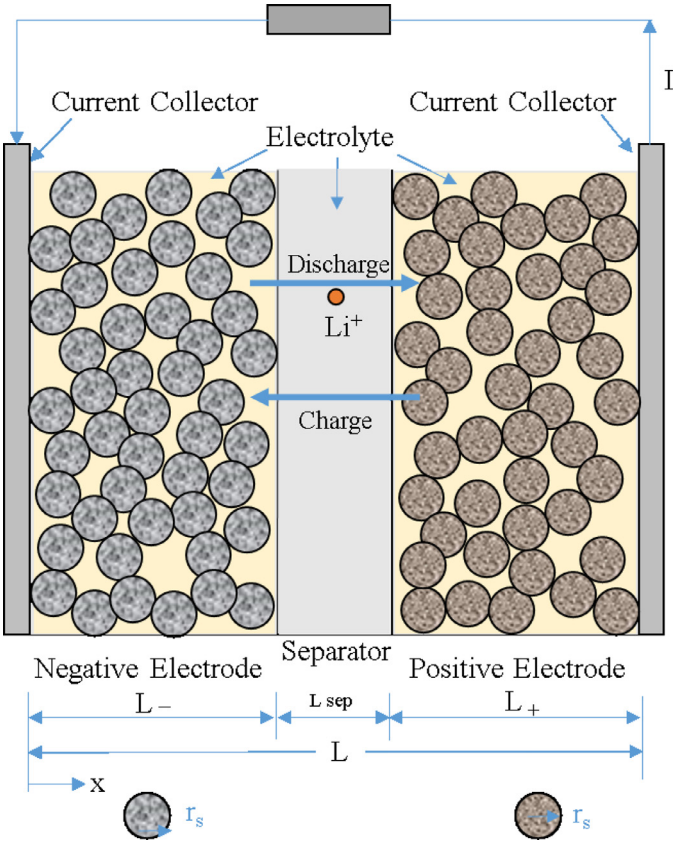

Fig. 1. Schematic of the lithium-ion battery cell modeled in the present study with the spatial x coordinate defined [24].

ature, while varying parameters to observe battery degradation, quantified the loss of capacity. Mathematically this entails solving the governing equations and degradation mechanisms associated with the key chemical reactions occurring during battery operation. Fig. 1 shows the domain modeled in the present study, that involves the negative and positive electrode and the separator separating the electrodes.

For a lithium-ion battery with a negative electrode active material of graphite, the reaction at the negative (or anode) electrode is as follows:

$$Li_nC_6 \rightleftharpoons C_6 + n\,Li^+ + n\,e^- \tag{1}$$

where the forward reaction represents the de-intercalation reaction (during discharge), and the backward reaction represents the intercalation reaction (during charge).

In this study, NMC (nickel-manganese-cobalt) cathodes are considered, and the reaction at the positive (cathode) electrode is represented by:

$$Ni_{1/3}Mn_{1/3}Co_{1/3}O_2 + m\,Li^+ + m\,e^- \rightleftharpoons Li_mNi_{1/3}Mn_{1/3}Co_{1/3}O_2 \tag{2}$$

where the forward reaction represents the intercalation reaction (during discharge), and the backward reaction represents the de-intercalation reaction (during charge).

2.1. Conservation equations

Before the governing equations are formulated, a thin and flat battery cell is considered, and a transient model is considered with one-dimensional dependence in the thickness of the battery cell for current distribution, concentrations and overpotential, with a given battery temperature; that is, temperature is assumed uniform for the entire cell and is specified in the present model. Therefore, the effect of battery temperature can be investigated as an independent parameter along with the discharge/charge cycling. Further, the only reactions occurring inside the battery cell are the intercalation/ deintercalation reactions at each electrode, and side reactions resulting in SEI film formation and growth (i.e., the SEI film thickening).

The governing equations that describe the physical and chemical processes occurring within the modeled domain are the solid-phase conservation of charge, electrolyte-phase conservation of charge, electrolye-phase Li^+ species concentration, the active material Li species conservation, and the Butler-Volmer equation for the electrode reactions at each of the electrodes. Further, the transport of electric charges is considered fast, so that quasi-steady assumption is employed. The model equations are presented below [24-26].

Solid-phase conservation of charge for the electrodes and the associated boundary conditions are:

$$0 = \frac{\partial}{\partial x}\left(\sigma_s^{\,eff}\frac{\partial \emptyset_s}{\partial x}\right) - j^{Li} \tag{3}$$

$$-\sigma_{s\_}^{\,eff}\frac{\partial \emptyset_s}{\partial x}\Big|_{x=0} = \sigma_{s+}^{\,eff}\frac{\partial \emptyset_s}{\partial x}\Big|_{x=L} = \frac{I}{A} \tag{4}$$

$$\frac{\partial \emptyset_s}{\partial x}\Big|_{x=L\_} = \frac{\partial \emptyset_s}{\partial x}\Big|_{x=L\_+L_{sep}} = 0 \tag{5}$$

$$\emptyset_s = \begin{cases} 0 & \text{at } x = 0 \\ V_{cell} & \text{at } x = L \end{cases} \tag{6}$$

where $\emptyset_s$ represents the electrical potential in the solid phase of the anode and cathode electrode, j^{Li} is the volumetric electrode current from all reactions, $\sigma_s^{\,eff}$ is the effective electrical conductivity of the given electrode material (hence, different for anode and cathode), A is the electrode's geometrical (or flat) surface area, and V_{cell} represents the cell voltage. Eq. (3) essentially describes the distribution of charge throughout the solid electrode, subject to some electrical production (or consumption) as a result of electrochemical reactions. Boundary Condition (4) indicates that the charge gradient at the boundary between the electrode material and current collector is linearly related to the current I drawn from the battery – this is the result of the assumption that the current density over the electrode surface is uniform for the present 1-D model (only variation in the thickness direction). Boundary Condition (5) indicates that the gradient of charge in the solid material is zero at either side of the separator, implying that no charge transfers through the separator as this is what the separator is intended for in Lithium-ion batteries.

Electrolyte-phase conservation of charge and the boundary conditions are:

$$0 = \frac{\partial}{\partial x}\left(\kappa^{eff}\frac{\partial \emptyset_e}{\partial x}\right) + \frac{\partial}{\partial x}\left(\kappa_D^{eff}\frac{\partial \ln(c_e)}{\partial x}\right) + j^{Li} \tag{7}$$

$$\frac{\partial \emptyset_e}{\partial x}\Big|_{x=0} = \frac{\partial \emptyset_e}{\partial x}\Big|_{x=L} = 0 \tag{8}$$

where $\emptyset_e$ is the electrical potential in the electrolyte phase, κ^{eff} is the effective ionic conductivity of the electrolyte, and κ_D^{eff} is the effective electrolyte diffusional conductivity. It should be noted that in the electrolyte phase, electrical potential is also governed by the diffusion of Li^+, hence its concentration (c_e). Similar to Eq. (3), Eq. (7) describes the distribution of charge throughout the electrolyte phase. In the solid phase, charge is transferred via electrons; however, in the electrolyte phase, charge is transferred through the movement of ions so that the distribution of charge is also influenced by the concentration gradient of lithium-ions (as is expressed in the second term of Eq. (7). Boundary Condition (8) indicates that the charge gradient at the boundary between the electrolyte and current collector is zero, indicating that charge is not transferred directly from the current collectors to the electrolyte (or vice versa). Note the electrolyte-phase conservation of charge

is solved continuously throughout the entire domain, including the separator layer.

Electrolyte-phase Li^+ species conservation, boundary and initial conditions:

$$\frac{\partial(\varepsilon c_e)}{\partial t} = \frac{\partial}{\partial x}\left(D_e^{eff}\frac{\partial c_e}{\partial x}\right) + \frac{1-t_+^0}{F}j^{Li} \tag{9}$$

$$\frac{\partial c_e}{\partial x}|_{x=0} = \frac{\partial c_e}{\partial x}|_{x=L} = 0 \tag{10}$$

$$c_e(t=0) = c_e^0 \tag{11}$$

where ε is the volume fraction of lithium in the electrolyte phase, D_e^{eff} is the electrolyte diffusion coefficient, and F the Faraday constant. Eq. (9) describes the distribution of lithium-ion concentration as it changes over time as a result of diffusion and electrochemical reactions. The last term in Eq. (9) describes the production (or consumption) of lithium-ions because of reactions at the electrodes. The boundary condition implies that lithium-ions cannot diffuse through the current collectors.

Electrode (solid) structure is composed of particles, as illustrated in Fig. 1; and using agglomerate model concept, Li species conservation (in particle radial direction) and the boundary conditions [23-26] are given as:

$$\frac{\partial c_s}{\partial t} = \frac{1}{r^2}\frac{\partial}{\partial r}\left(D_s r^2 \frac{\partial c_s}{\partial r}\right) \tag{12}$$

$$\frac{\partial c_s}{\partial r}|_{r=0} = 0 \tag{13}$$

$$-D_s\frac{\partial c_s}{\partial r}|_{r=r_s} = \frac{j^{Li}}{a_s F} \tag{14}$$

$$c_s(t=0) = c_s^0 \tag{15}$$

where c_s is the concentration of lithium in the solid phase (electrode material), D_s is the lithium diffusion coefficient in the solid phase, and a_s is the specific interfacial area between the solid and electrolyte phase in an electrode. The above equations describe the concentration of Li in the solid particles (c_s). Note that the Li species conservation in the active material (solid phase) is considered in the radial direction, describing the Li species conservation in a particle of active material. Boundary Condition (13) is a symmetry condition applied at the center of the particle, and Boundary Condition (14) describes the process of lithium-ions being consumed (or produced) at the particle boundary causing lithium to be inserted (or removed) from the electrode material as a result of electrochemical reactions.

Finally, the Butler-Volmer equation is applied at each electrode to model the reaction rates of the lithium intercalation reactions:

$$j^{IC} = a_s j_o^{IC}\left\{\exp\left[\frac{\alpha_a F}{RT}\left(\eta - \frac{R_f}{a_s}j^{Li}\right)\right] - \exp\left[-\frac{\alpha_c F}{RT}\left(\eta - \frac{R_f}{a_s}j^{Li}\right)\right]\right\} \tag{16}$$

where R and T are the universal gas constant and battery operation temperature, respectively; α_a and α_c the anodic and cathodic transfer coefficients (both taken to be 0.5 at both electrodes); R_f the SEI film resistance at the given electrode; j_o^{IC} the exchange current density, and η the local surface overpotential, defined as follows

$$\eta = \emptyset_s - \emptyset_e - U \tag{17}$$

where U is the open-circuit voltage. It is important to note that j^{IC} represents the volumetric electrode current due to intercalation reactions only (not taking into account side reactions), and it is related to j^{Li}, the total volumetric electrode current from all reactions:

$$j^{Li} = j^{IC} + i_s a_s \tag{18}$$

where i_s is the side reaction current density, arising from the side reactions occurring at the electrode that lead to the degradation of electrode performance (hence the entire cell performance as well, that is, the source of the performance loss or capacity fade), as described in the next subsection.

2.2. Modelling of degradation mechanisms

Mechanisms of performance degradation have been investigated in literature, and summarized in a recent review article [23], and the degradation submodel is developed based on [23, 26, 27]. Around and above room temperature, there exist two major degradation mechanisms: SEI film formation and growth around the electrode solid particles at each of the electrodes, and loss of active material for both electrodes. Before the formation and growth of the SEI film, ethylene carbonate (EC) must diffuse through the SEI layer to the interface between the SEI film and the electrolyte; and this diffusion process is represented by the following equation:

$$\frac{\partial c_{EC}}{\partial t} = D_{EC}^{eff}\frac{\partial^2 c_{EC}}{\partial r^2} \tag{19}$$

where D_{EC}^{eff} is an effective diffusivity accounting for the tortuosity of the path through the porous SEI layer.

The SEI formation and growth occurs at the interface between the carbon particles and the exiting SEI layer, arising from the following reaction to produce lithium alkyl carbonate ($(CH_2OCO_2Li)_2$):

$$2(CH_2O)_2CO + 2e^- + 2Li^+ \rightarrow (CH_2OCO_2Li)_2 + C_2H_4 \tag{20}$$

The rate of the reaction is expressed as follows:

$$i_{s,A} = -i_{0s,A}\exp\left[\frac{\alpha_{s,A}F}{R_u T}(\phi_s - \phi_e - R_{SEI}i_{t,A})\right] \tag{21}$$

$$i_{t,A} = \frac{j^{Li}}{a_s} \tag{22}$$

here $i_{s,A}$ is the side reaction current density per unit surface area at the anode, which is related to the volumetric electrode current as seen in Eq. (18) for the anode electrode; while $i_{t,A}$ is the total current density of both intercalation and the side reactions at the anode. $i_{0s,A}$ is the exchange current density for the side reaction and is related to the concentration of ethylene carbonate (EC) at the reaction surface, c_{EC}^s, and reaction rate constant, $k_{s,A}$, specified using an Arrhenius relation with a defined activation energy E and reference rate constant $k_{s,A,0}$:

$$i_{0s,A} = Fk_{s,A}c_{EC}^s \tag{23}$$

$$k_{s,A} = k_{s,A,0}\exp\left(-\frac{E}{RT}\right) \tag{24}$$

Then the growth of the SEI layer is determined by

$$\frac{\partial \delta_{SEI}}{\partial t} = \frac{-i_{s,A}}{2F}\frac{M_{SEI}}{\rho_{SEI}} \tag{25}$$

where δ_{SEI} is the SEI layer thickness, M_{SEI} and ρ_{SEI} are the molecular weight and density of the SEI layer, respectively. The resistance of the SEI layer is then estimated by

$$R_{SEI} = \frac{\delta_{SEI}}{\kappa_{SEI}^{eff}} \tag{26}$$

where κ_{SEI}^{eff} is the effective conductivity of the electrolyte through the SEI layer, again accounting for the tortuous path through the porous SEI layer.

A similar model is developed for film formation and growth at the cathode. To describe diffusion of EC through the layer, Eq. (19) is used again, with corresponding parameters for the cathode. The reaction describing the production of the SEI film around solid particles for an NMC cathode is as follows:

$$Li(Ni, Co)O_2 + ROCO_2R' \rightarrow (Ni, Co)O_2R + R'OCO_2Li \tag{27}$$

where R' is a radical, and the rate of reaction can be written as:

$$i_{s,c} = k_{s,C} c_{EC,s} c_{Li(Ni,Co)O_2} \tag{28}$$

Here $i_{s,c}$ represents the side reaction rate per unit surface area of the cathode electrode, $c_{EC,s}$ is the EC concentration at the particle surface, and $c_{Lix(Ni,Co)O_2}$ is the cathode material concentration, and $k_{s,C}$ is a rate constant specified using an Arrhenius relation with a defined activation energy and reference rate constant, similar to Eq. (24). The growth of the film can then be described as follows:

$$\frac{\partial \delta_{film}}{\partial t} = \frac{i_{s,C}}{F} \frac{M_{film}}{\rho_{film}} \tag{29}$$

The SEI film resistance can be calculated in the same manner as that given in Eq. (25).

Another source of degradation is the loss of active material. This mechanism takes into account particles of active material that over time have detached from the binder, and no longer serve as an active material site. This detachment is attributed to mechanical stresses caused by volume changes during cycling, and can be modelled using a simple relation between the rate of material isolation and the electrode current from reaction:

$$\frac{\partial \varepsilon_{AM}}{\partial t} = -k(T)\left|j^{Li}\right| \tag{30}$$

Here ε_{AM} represents the volume fraction of the active material in each of the electrodes, k(T) is the rate constant defined by an Arrhenius relation with a specified activation energy and reference rate constant, similar to Eq. (24) shown earlier.

2.3. Numerical Implementation

As pointed out earlier, in this study temperature is specified for the battery operation, acting as an independent parameter; properties and current distribution, concentration, and overpotential are assumed variable only in the thickness direction of the battery cell. Therefore the solid-phase conservation of charge, electrolyte-phase conservation of charge, and conservation of electrolyte-phase Li^+ species are all discretized once in space through the thickness of the cell (normal to the cell height). The conservation of Li species in the active material is discretized in the radial direction of a particle of the active material, following the particle assumption of the solid phases in the electrodes. All these equations are discretized in space and solved utilizing a finite control volume method; explicit scheme is used for the time-marching. To utilize the various property information, the software package AutoLionST [26] is utilized for the numerical solution. A mesh refinement study indicates that it is sufficient to use 8 finite volumes in both the positive and negative electrodes, 8 volumes in the solid particle, and 5 volumes in the separator, with further numerical details available elsewhere [28].

3. Experimental

The battery used is a pouch-cell with aluminum packaging of dimensions 11 × 60 × 162 mm in the thickness, width and height direction, respectively; with a carbon anode, NMC cathode, and a polymer separator. Additional information is available [29], although the exact specifics of the battery chemistry are proprietary [30], like most of commercial Lithium-ion batteries. The battery rated capacity is 10Ah (± 0.5Ah), with a charge cut-off voltage of 4.2 V and a discharge cut-off voltage of 2.75 V. The battery used for model calculation is taken to reflect the battery studied experimentally, with the proprietary battery chemistry information being available in the software package AutoLionST [26], a major reason in implementing the model calculation in this software package platform.

Isothermal experiments are performed. The battery is fully discharged from 4.2 V to 2.75 V at a rate of 1C (10A), and charged using a 1C constant-current-constant-voltage (CCCV) load profile. Between each discharge (or charge) and charge (or discharge) the battery is rested for 5 min. As the battery is cycled, battery capacity is recorded. Since battery operation is sensitive to thermal conditions, it is desired that battery temperature be controlled during this experiment. Based on the advice from our industry partners, it is decided that these experiments take place at a moderately elevated temperature of 35°C.

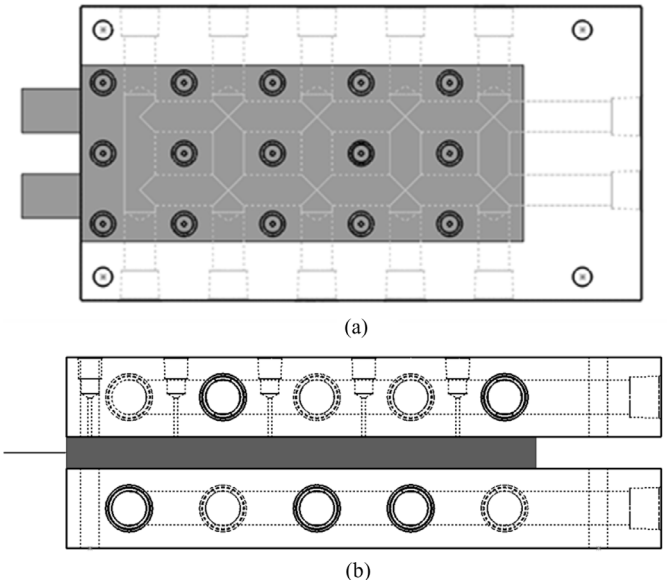

Fig. 2. Schematic of the thermal plate heat exchangers used for battery temperature control, showing heating fluid flow channel and thermocouple locations relative to the test battery (a) top view; (b) side view.

An experimental apparatus is set up to cycle batteries over long periods, and record capacity data. The experiments are performed using an *Emerald-Advanced Battery Test Station* by *Greenlight Innovation* to repeatedly discharge and charge a battery over an extended period of time [31]. The battery test station also records extensive data related to the test condition and battery performance, and monitors the health of battery during operation. The test station records accumulated charge as the battery is in operation which represents the charge (in Ah) that the battery supplies. Hence, the accumulated charge at the end of discharge is the true capacity that the battery delivers, which is the data of interest.

Battery temperature is controlled through the use of thermal control plates (plate heat exchangers) to hold the battery at near-isothermal conditions. Two aluminum (thermal) plates are designed to control temperature on both sides of the battery; both plates featured identical $\frac{1}{4}$ NPT tapped channels to control temperature by the use of a working fluid. Fig. 2 shows the top and side views of the plates to show the manifold design in relation to the size and location of the battery. The aluminum plates are used to ensure good thermal conductivity, and they are larger than the battery so that the area of flow channels machined on the aluminum plates covers the battery surface area to ensure proper surface temperature of the battery under test.

The heating flow channels on both aluminum plates are connected to a *Thermo Scientific A 25B* thermal bath [32] supplying a 50/50 mixture of water and ethylene glycol circulated by a *Thermo Scientific AC200 Immersion Circulator* [33] at a flow rate of 20 L/min (10 L/min per plate) through tubing of 5/16″ I.D. The specified working fluid and flow rate results in a mass flow rate of approximately 0.4 kg/s. The battery surface temperature is monitored by *Labview* using an array of 15 T-type *Omega* thermocouples, held in place using *Swagelok* brass tube fittings. The standard limits for error for the T-type thermocouples is ±1 °C [34]. The two thermal plates are held parallel to each other using four bolts; springs are also set below the bottom thermal plate to ensure good con-

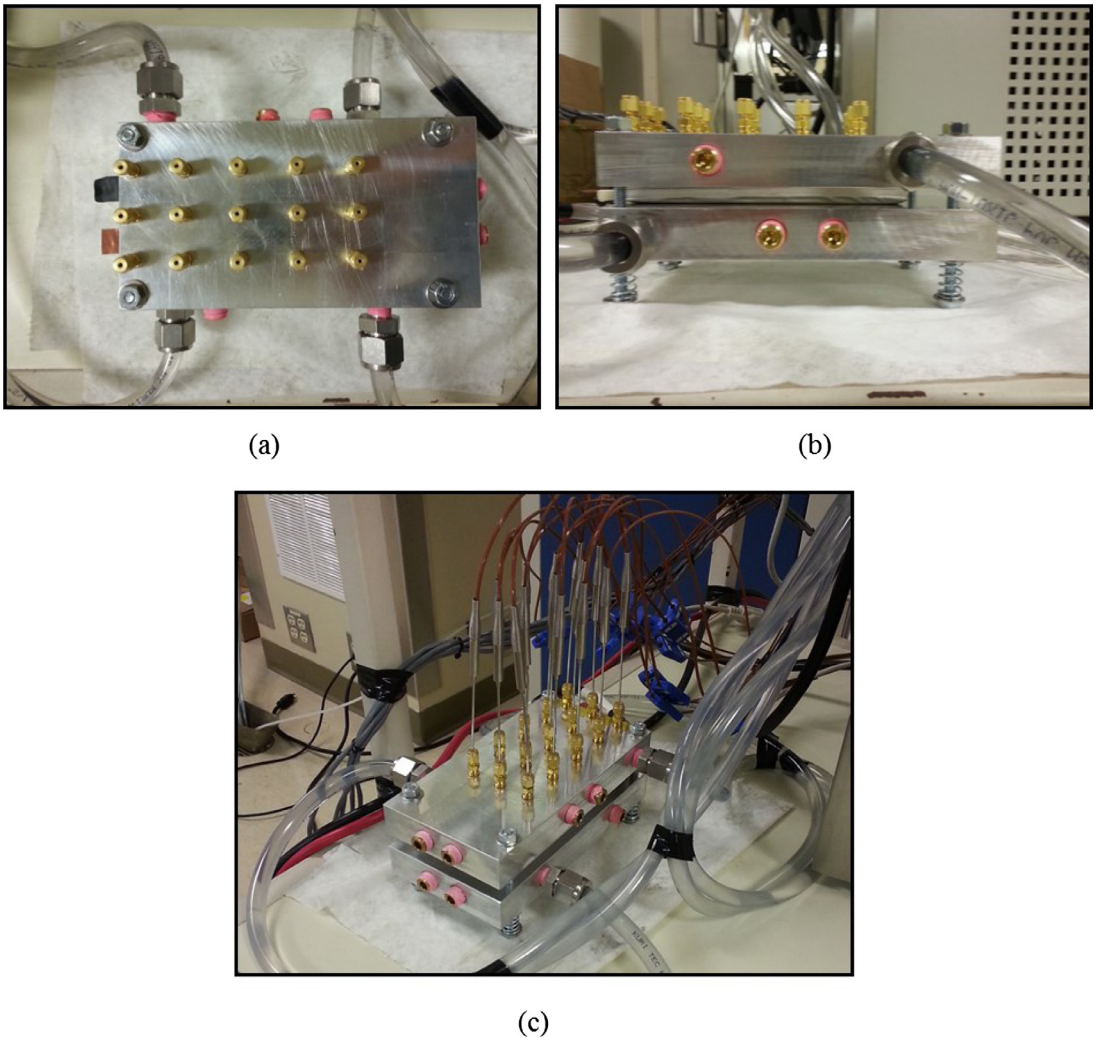

Fig. 3. Experimental setup for battery capacity test; (a) top view: thermally-regulated inlets/outlets and thermocouple fittings are seen; (b) side view: battery can be seen between plates; (c) full setup including thermocouples connected in place.

tact between the plates and battery while also allowing for any expansion. Fig. 3 depicts the thermal plates, and the full experimental set up.

The thermocouples are in contact with the battery surface by firmly pressing them against the battery surface with the use of the pressure fittings. The entire weight of the top thermal plate rests on the battery with the thermocouples pressure fit to the thermal plate; as such, it is assumed that there is good thermal contact between the battery and thermocouples.

4. Results and discussion

As described earlier, a battery is discharged at 1C from the charge cut-off voltage of 4.2 V to the discharge cut-off voltage of 2.75 V, then the battery is charged back to a voltage of 4.2 V using again at 1C, using CCCV charging procedure. During CCCV charging, the CV phase is performed by slowly stepping down the current (in steps of 1A) to ensure the battery voltage is maintained at 4.2 V for each current step. Between each discharge/charge and charge/discharge the battery is rested for 5 min. During the test for both charge/discharge process, the battery temperature is maintained at 35 °C, using the plate heat exchangers with heating fluid from the thermal bath as described earlier.

Fig. 4 shows the comparison between the battery voltage and current profiles during the discharge and charge process for the experimental and model predicted results. It is seen in Fig. 4(a) that as the battery is discharged, the battery current drops right away to the set value corresponding to the 1C discharge rate; while the battery voltage is reduced gradually, until towards the end of the discharge period that the voltage is decreased steeply to the discharge cut-off voltage of 2.75 V. Fig. 4(b) indicates that for the charge process, the charge current is maintained at a constant and high value while the battery voltage is increased; once the battery voltage reaches the charge cut-off voltage of 4.2 V, the charge current is reduced gradually to maintain the battery voltage constant to avoid overcharge that may lead into overheating, which may cause fire and explosion hazards [23]. It might be mentioned that the model predicted results for the battery performance shown in Fig. 4 are obtained by solving the governing conservation equations coupled with the degradation submodels as formulated earlier. It is evident that reasonable agreement is obtained for both battery current and voltage during both discharge and charge time, although the model predicted voltage is slightly higher than the corresponding experimental results of the battery voltage for the discharge process.

The model predicted results for the battery capacity are obtained by solving the governing conservation equations, along with the degradation mechanisms considering the growth of SEI layers and the loss of active materials in both anode and cathode electrodes. Table 1 shows the corresponding kinetic parameters for the degradation sub-model used in the model calculations. It should be mentioned that these kinetic pa-

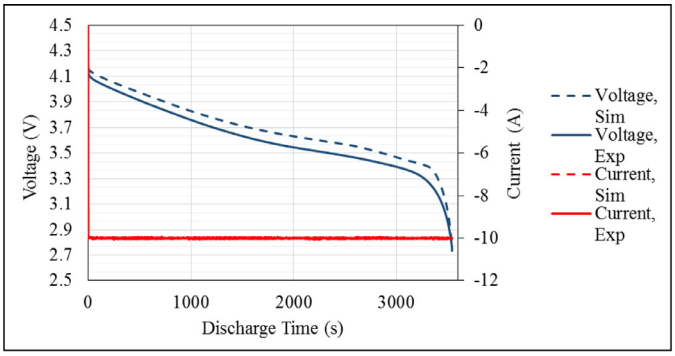

(a) Discharge Process

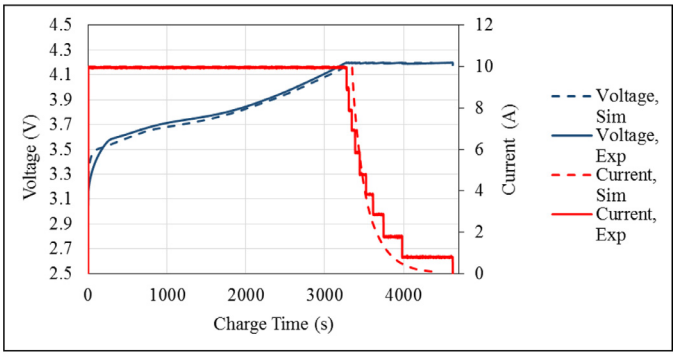

(b) Charge Process

Fig. 4. Comparison of model predicted (curves indicated by "Sim") and experimentally measured (curves indicated by "Exp") battery cell voltage and current profiles during (a) discharge period; (b) charge period. The red color lines denote the current (negative in discharge and positive in charge process), and the blue color lines are the voltage. (For interpretation of the references to color in this figure legend, the reader is referred to the web version of this article.)

Table 1
Degradation kinetic parameters used in the present model calculations. The reaction rate constants shown in Eqs. (23), (28) and (30) are expressed in the Arrhenius form of Eq. (24) as follows: $k = k_0 \exp\left(-\frac{E}{RT}\right)$ where the reference reaction rate constant (or the pre-exponential term) k_0 and the activation energy E used in the present study are shown in this table.

	Parameter Values	Units
Negative Electrode SEI Film Growth		
Reference Rate Constant	1.30×10^{-18}	m/s
Activation Energy	8.53×10^{4}	J/mol
Positive Electrode SEI Film Growth		
Reference Rate Constant	3.1×10^{-8}	m/s
Activation Energy	2.5×10^{4}	J/mol
Negative Electrode Active Material Isolation (AMI)		
Reference Rate Constant	3.47×10^{-14}	m/s
Activation Energy	4×10^{4}	J/mol
Positive Electrode Active Material Isolation (AMI)		
Reference Rate Constant	0	m/s
Activation Energy	3×10^{4}	J/mol

rameters shown in Table 1 were obtained based on the experimental results through data-driven analysis that minimized the difference between the predictions and experimental outcomes. This approach can be used for on-going update of the kinetic parameters through online monitoring of the practical battery in operation as well, thus providing real-time prediction of the battery capacity fade in practice. Experimental results for battery capacity at the end of each discharge/charge phase are measured by the battery test station. Over the first 10 cycles, the average battery surface temperature is 34.6 °C with a standard deviation of 0.03 °C. The maximum spatial surface temperature difference within a single time step is 0.42 °C, with an average spatial temperature difference of 0.32 °C throughout all time steps encountered during the test. This 10 cycle result indicates the performance of the plate heat exchangers used in the present study to maintain the constant battery temperature during the discharge/charge cycling process, and is representative of the battery temperature during the cycling process for the measurement of the battery capacity change as the number of cycle is increased.

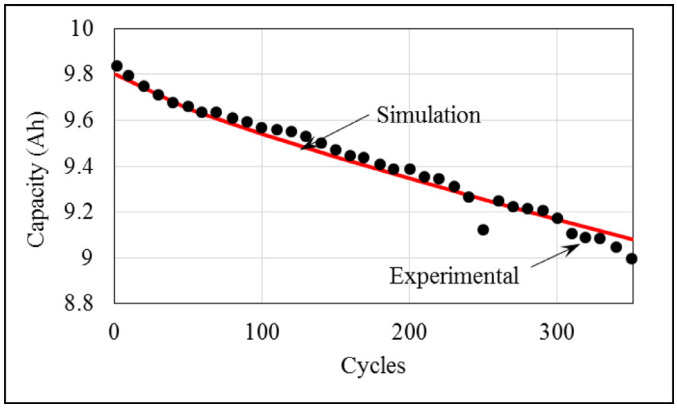

Fig. 5. Comparison between the model predicted and experimental battery capacity at 1C charge/discharge cycling at the battery operation temperature of 35 °C.

A comparison of the model predicted results against the experimental data for the battery capacity at 1C discharge/charge is shown in Fig. 5. It is seen that as the number of the battery discharge and charge cycles are increased, the capacity is reduced steadily. The slope of reduction is the largest for the first 40 cycles or so, and then seems to slow down to a smaller slope until about 300 cycles before the capacity fade is accelerated with a steeper slope. It is further noticed that the model prediction agrees reasonably well with the experimental results. Recall that the capacity reduction (or fade) is attributed to the SEI film formation and growth, and the loss of active materials, in both the negative and positive electrodes. For the given condition of battery temperature of 35 °C and discharge/charge rate at 1C investigated, the degradation mechanisms seem to capture the capacity degradation well as the number of discharge/charge cycles is increased. Therefore, it might be considered that the model formulated in the present study might be regarded as validated reasonably. It might be mentioned that from the model results the largest contributing factor to the capacity fade is due to SEI film growth at the negative electrode, with the active material isolation at the negative electrode being the second largest, and these two factors constitute the majority of the capacity fade.

Following the validation, the present model is used to predict capacity degradation for other battery operation temperatures, as shown in Fig. 6. The model prediction is calculated using the same procedure as before; fully discharged at 1C, then fully charged at 1C using CCCV charging, while the battery is considered isothermal at a specified operation temperature. The battery operation temperature is then varied from 20 °C to 60 °C in order to assess the effect of battery operation temperature on the capacity fade. Other mechanisms become important if the battery temperature becomes lower [23]. Fig. 6(a) presents the model predicted capacity change with the number of discharge and charge cycles. It is seen that as the battery operation temperature is increased, the initial battery capacity at the beginning of the cycling is increased. For a given battery temperature, the capacity decrease becomes steeper with larger slope for the decrease, such that at the battery temperature of 20 °C, the battery can experience almost 2000 cycles before its capacity is reduced to 7.5 Ah; but at the increased temperature of 60 °C,

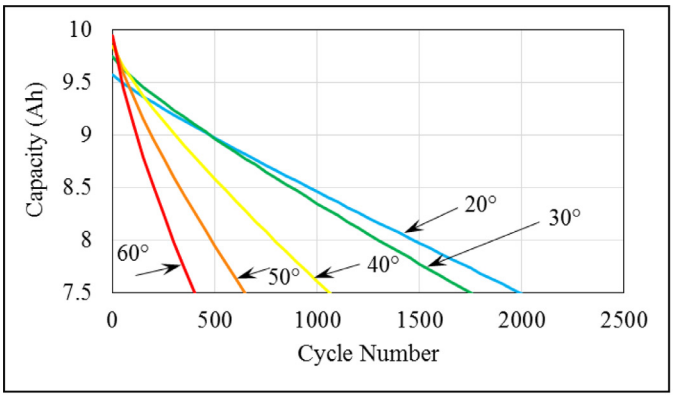

(a) Capacity

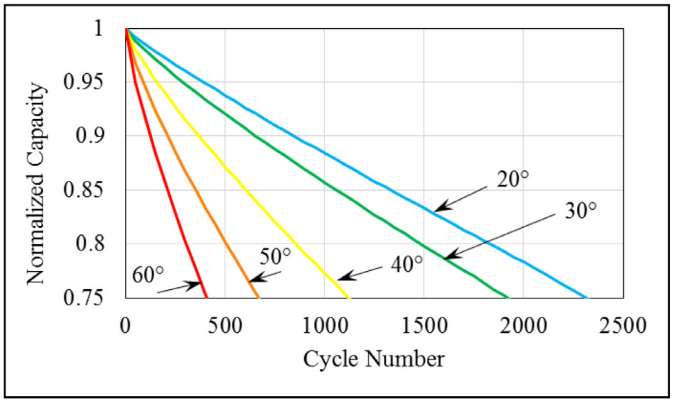

(b) Normalized Capacity

Fig. 6. Degradation of battery capacity as a function of the discharge and charge cycles for isothermal discharge/charge rate at 1C at various battery operation temperatures as indicated: (a) capacity; (b) normalized capacity.

it only takes about 400 discharge/charge cycles for the capacity to be decreased to the same level of 7.5 Ah. This illustrates the importance of battery thermal management in enhancing the lifetime of battery, and thermal management becomes even more important considering that batteries in automobiles can experience even higher temperatures during the summer under sunshine for many parts of the world. Fig. 6(b) shows the variation of the capacity normalized by its initial value; this representation is advantageous in estimating the battery lifetime since typically battery in an electric vehicle is considered reaching its end of useful life if the battery capacity is reduced to 75% of its original (new battery capacity) value. It is clear the battery considered in this study can have a life of over 2300 discharge/charge cycles at the battery operation temperature of 20 °C; becomes just over 1000 cycles at 50 °C, and less than 500 cycles at 60 °C. It is clear that battery capacity is reduced substantially with the number of the discharge/charge cycles, indicating significantly accelerated aging of the battery at elevated operation temperatures. Therefore, a good battery thermal management system is essential to maintain battery operational lifetime for electric vehicle applications.

5. Conclusions

In this study, a first-principles based predictive model has been developed for the operation and degradation of a lithium-ion battery. The mechanisms of degradation considered include solid-electrolyte interface (SEI) formation and growth as well as active material loss (or isolation) at both negative and positive electrodes. Experiments are conducted to measure the battery performance under discharge and charge cycling at isothermal condition with battery operation temperature controlled through two plate heat exchangers. It is shown that battery capacity is reduced over battery discharge/charge cycling at a given battery operation temperature, and the model predicted battery performance, especially performance degradation (capacity fade), agrees well with the experimental results. This validated model can provide predictive results about the battery capacity fade and lifetime under various operating conditions, saving time and expense associated for similar experimental measurements. As the number of discharge/charge cycles are increased, battery capacity is reduced significantly; battery capacity fade is increased substantially when battery operation temperature is increased, indicating significantly accelerated aging of the battery at elevated operation temperatures and hence the importance of battery thermal management in the control of battery operation temperature for practical applications such as electric vehicles. Battery capacity fade is mainly caused by SEI film growth at the negative electrode, which is the largest contributing factor to the capacity fade, and the active material isolation at the negative electrode, which is the second largest influencing aging factor.

Declaration of Competing Interest

The authors declare that they have no known competing financial interests or personal relationships that could have appeared to influence the work reported in this paper.

Acknowledgement

This work has received financial support from the Natural Sciences and Engineering Research Council of Canada (NSERC) via an Engage Grant with the grant number EGP 483882–15, and a Discovery Grant. The Engage Grant was also co-sponsored by Dana Canada Corporation.

References

[1] Lu L, Han X, Li J, Hu J, Ouyang M. A review on the key issues for lithium-ion battery management in electric vehicles. J Power Sources 2013;226:272–88.
[2] Scrosati B, Garche J. Lithium batteries: status, prospects and future. J Power Sources 2010;195:2419–30.
[3] Linden D, Reddy TB. Handbook of batteries. Third Edition. McGraw-Hill Inc.; 2002.
[4] Wang Q, Ping P, Zhao X, Chu G, Sun J, Chen C. Thermal runaway caused fire and explosion of lithium ion battery. J Power Sources 2012;208:210–24.
[5] Arora P, White RE, Doyle M. Capacity fade mechanisms and side reactions in lithium-ion batteries. J Electrochem Soc 1998;145:3647–67.
[6] Fong R, von Sacken U, Dohn JR. Studies of Lithium Intercalation into carbons using nonaqueous electrochemical cells. J Electrochem Soc 1990;137:2009–13.
[7] Aurbach D, Zinigrad E, Cohen Y, Teller H. A short review of failure mechanisms of lithium metal and lithiated graphite anodes in liquid electrolyte solutions. Solid State Ion 2002;148:405–16.
[8] Broussely M, Biensan Ph, Bonhomme F, Blanchard P, Herreyre S, Nechev K, Staniewicz RJ. Main aging mechanisms in Li ion batteries. J Power Sources 2005;146:90–6.
[9] Vetter J, Novak P, Wagner MR, Veit C, Moller K-C, Besenhard JO, Winter M, Wohlfahrt-Mehrens M, Vogler C, Hammouche A. Ageing mechanisms in lithium-ion batteries. J Power Sources 2005;147:269–81.
[10] Bro P, Levy SC. Quality and reliability methods for primary batteries. John Wiley & Sons Inc; 1990.
[11] Ramadass P, Haran B, White R, Popov BN. Capacity fade of Sony 18650 cells cycled at elevated temperatures Part I. Cycling performance. J Power Sources 2002;112:606–13.
[12] Ramadass P, Haran B, White R, Popov BN. Capacity fade of Sony 18650 cells cycled at elevated temperatures Part II. Capacity fade analysis. J Power Sources 2002;112:614–20.
[13] Ramadass P, Haran B, White R, Popov BN. Mathematical modeling of the capacity fade of Li-ion cells. J Power Sources 2003;123:230–40.
[14] Broussely M, Herreyre S, Biensan P, Kasztejna P, Nechev K, Staniweicz RJ. Aging mechanisms in Li ion cells and calendar life predictions. J Power Sources 2001;97-98:13–21.
[15] Spotnitz R. Simulation of capacity fade in lithium-ion batteries. J Power Sources 2003;113:72–80.
[16] Liaw BY, Jungst RG, Nagasubramanian G, Case HL, Doughty DH. Modeling capacity fade in lithium-ion cells. J Power Sources 2005;140:157–61.
[17] Ramadass P, Haran B, Gomadam PM, White R, Popov BN. Development of first principles capacity fade model for Li-ion cells. J Electrochem Soc 2004;151:A196–203.
[18] Vazquez-Arenas J, Fowler M, Mao X, Chen S. Modeling of combined capacity fade with thermal effects for a cycled Li_xC_6-$Li_yMn_2O_4$ cell. J. of Power Sources 2012;215:28–35.

[19] Deshpande R, Verbrugge M, Cheng Y-T, Wang J, Liu P. Battery cycle life prediction with coupled chemical degradation and fatigue mechanics. J Electrochem Soc 2012;159:A1730–8.
[20] Cai L, Dai Y, Nicholson M, White RE, Jagannathan K, Bhatia G. Life modeling of lithium ion cell with a spinel-based cathode. J. of Power Sources 2013;221:191–200.
[21] Smith AJ, Burns JC, Zhao X, Xiong D, Dahn JR. A high precision coulemetry study of the SEI growth in Li/graphite cells. J Electrochem Soc 2011;158:A447–52.
[22] Amine K, Chen Z, Zhang Z, Kiu J, Lu W, Qin Y, Ju J, Curtis L, Sun Y-K. Mechanism of capacity fade of MCMB/$Li_{1.1}[Ni_{1/3}Mn_{1/3}Co_{1/3}]_{0.9}O_2$ cell at elevated temperature and additives to improve its cycle life. J Mater Chem 2011;21:17754–9.
[23] Han X, Lu L, Zheng Y, Feng X, Li Z, Li J, Ouyang M. A review on the key issues of the lithium ion battery degradation among the whole life cycle. eTransportation 2019;1(1-21):100005.
[24] Fang W, Kwon OJ, Wang CY. Electrochemical-thermal modeling of automotive Li-ion batteries and experimental validation using a three-electrode cell. Int J Energy Res 2010;34:107–15.
[25] Doyle M, Fuller TF, Newman J. Modeling of galvanostatic charge and discharge of the Lithium/polymer/insertion cell. J Electrochem Soc 1993;140:1526–33.
[26] E.C. Power. AutoLionST: a thermally coupled battery model for system-level analysis of li-ion battery packs. User's Manual, 2015.
[27] Safari M, Morcrette M, Teyssot A, Delacourt C. Multimodal physics-based aging model for life prediction of Li-ion batteries. J Electrochem Soc 2009;156:A145–53.
[28] Carnovale A. Investigation into the effect of thermal management on the capacity fade of lithium-ion batteries MASc thesis. University of Waterloo; 2016.
[29] AA Portable Power Corp, M. Liu. Polymer lithium-ion battery product specification, Model:10059156-5C. 2012.
[30] AA Portable Power Corp. Polymer lithium-ion battery safety data sheets. 2012.
[31] Emerald-ABT: test control software for advanced battery testing user manual. Greenlight Innovation; 2012.
[32] Laboratory temperature control products. Thermo Scientific; 2010.
[33] AC200 immersion circulators. ThermoFisher Scientific; 2016. Retrieved from https://www.thermofisher.com/order/catalog/product/156-0001.
[34] Thermocouples: using thermocouples in temperature measurement. OMEGA; 2016. Retrieved from http://www.omega.ca/prodinfo/thermocouples.html.